Validated Analysis of Component Distribution Inside Perovskite Solar Cells and Its Utility in Unveiling Factors of Device Performance and Degradation

Cheng-Hung Hou, Shu-Han Hung, Li-Ji Jhang, Keh-Jiunh Chou, Yu-Kai Hu, Pi-Tai Chou, Wei-Fang Su, Feng-Yu Tsai, Jay Shieh, and Jing-Jong Shyue*

Cite This: *ACS Appl. Mater. Interfaces* 2020, 12, 22730−22740

Read Online

ACCESS | Metrics & More | Article Recommendations | SI Supporting Information

ABSTRACT: Time-of-flight secondary-ion mass spectrometry (ToF-SIMS) has been used for gaining insights into perovskite solar cells (PSCs). However, the importance of selecting ion beam parameters to eliminate artifacts in the resulting depth profile is often overlooked. In this work, significant artifacts were identified with commonly applied sputter sources, i.e., an O_2^+ beam and an Ar-gas cluster ion beam (Ar-GCIB), which could lead to misinterpretation of the PSC structure. On the other hand, polyatomic C_{60}^+ and Ar^+ ion beams were found to be able to produce depth profiles that properly reflect the distribution of the components. On the basis of this validated method, differences in component distribution, depending on the fabrication processes, were identified and discussed. The solvent-engineering process yielded a homogeneous film with higher device performance, but sequential deposition led to a perovskite layer sandwiched by methylammonium-deficient layers that impeded the performance. For device degradation, it was found that most components remained intact at their original position except for iodide. This result unambiguously indicated that iodide diffusion was one of the key factors governing the device lifetime. With the validated parameters provided, ToF-SIMS was demonstrated as a powerful tool to unveil the structure variation amid device performance and during degradation, which are crucial for the future development of PSCs.

KEYWORDS: ToF-SIMS, perovskite solar cell, depth profile, cluster ion, degradation

INTRODUCTION

The discovery of metal halide perovskite materials has a tremendous influence on the photovoltaic (PV) community. An unprecedented growth of the power conversion efficiency (PCE) of perovskite solar cells (PSCs) has been achieved in a short time span.[1−3] In addition to their high PCEs, there are a number of advantages that make PSC a transformative technology, including the facile solution processes for depositing the perovskite layers[4,5] and the composition tunability.[6−8] These features have contributed to the low-cost manufacturing and tunable absorption of PSCs, which enable an effective approach to boost the efficiency of solar cells.[9−11] However, the flexibility of PSCs also makes the development of a robust approach that produces the desired film morphology difficult. In addition to the uniformity and surface roughness, the stoichiometry[12,13] and component distribution[14,15] of the perovskite film are also the governing factors that influence the device performance. An analytical tool that enables accurate determination of the component distribution inside the film is therefore crucial for promoting PSC technology, especially for perovskite materials with multiple components.[7,9,10]
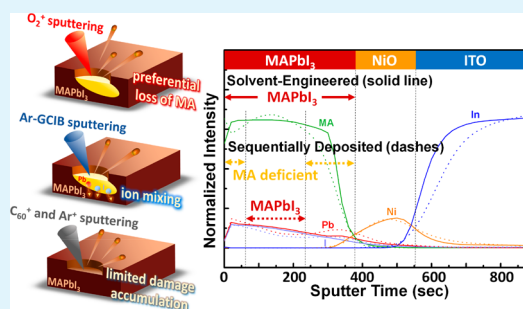
Time-of-flight secondary-ion mass spectrometry (ToF-SIMS) is one of the few techniques that provides comprehensive information about film composition, including identification of molecular components and their spatial distributions. In previous studies, the utility of ToF-SIMS in revealing the bulk and the interface nature of perovskite films was demonstrated, such as the observation of a subtle change in the film composition[16,17] and mobile ions in PSCs.[18−21] During ToF-SIMS analysis, the investigated film is bombarded by primary ions (PIs), which then generates secondary ions (SIs) from the outermost surface after a collision cascade. To achieve a high signal intensity during ToF-SIMS analysis, various procedures have been developed to increase the SI yields. One effective approach is applying O_2^+ sputtering or O_2 flooding. When the sample surface is partially oxidized,
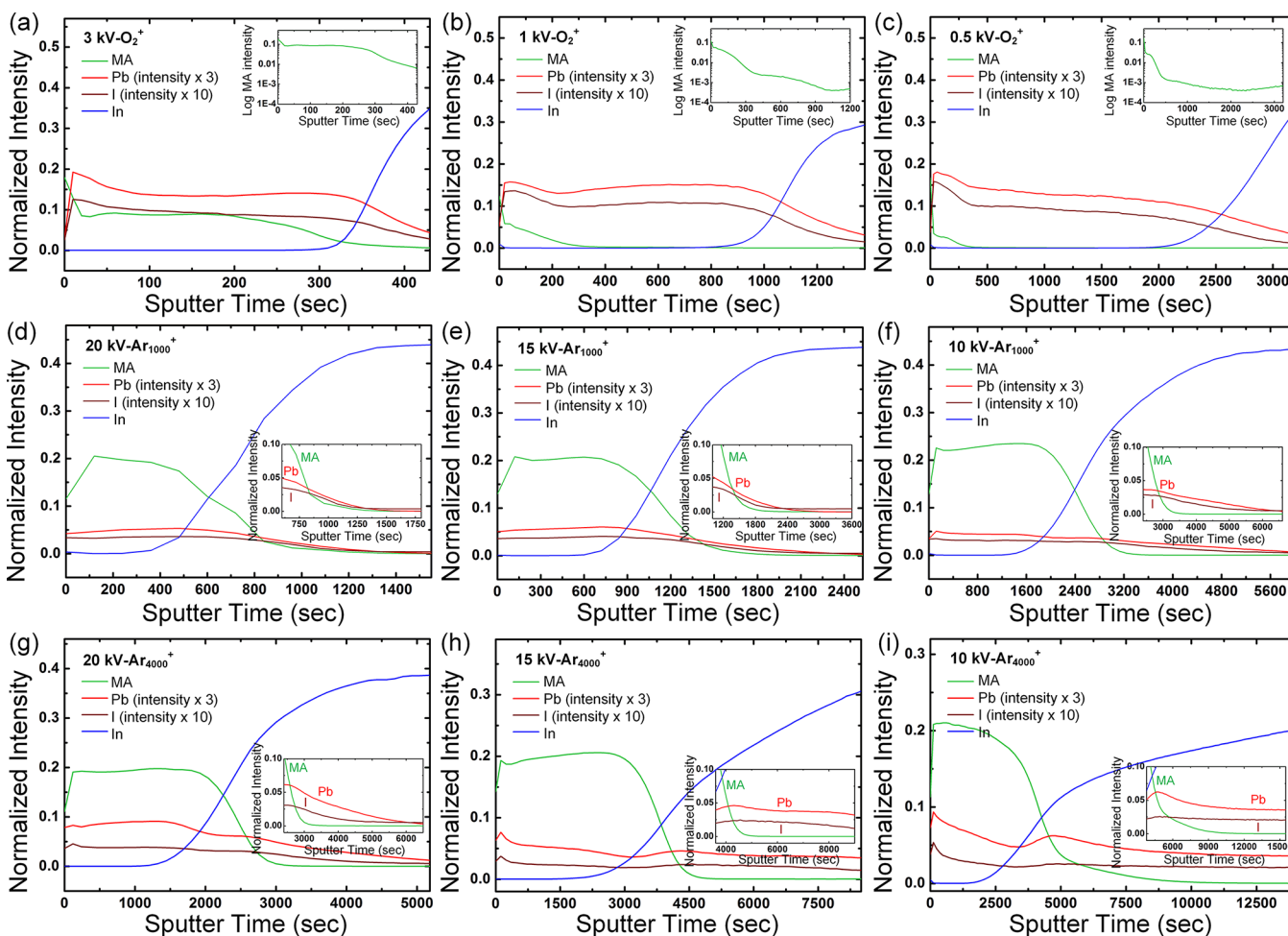
Figure 1. ToF-SIMS depth profiles (normalized with respect to the total ion count of each acquisition) of a solvent-engineered MAPbI$_3$ film on the ITO substrate: (a) 3, (b) 1, and (c) 0.5 kV O$_2{}^+$; (d) 20, (e) 15, and (f) 10 kV Ar$_{1000}{}^+$; (g) 20, (h) 15, and (i) 10 kV Ar$_{4000}{}^+$ sputtering.

neutralization of SI is suppressed; hence, it facilitates the emission of positive ions.[22] On the basis of a similar concept, the intensity of negative SI can also be enhanced by Cs$^+$ sputtering or flooding.[23] With the Cs$^+$ sputtering, the so-called MCs$^+$ technique[24] can also be used to detect electronegative species as compound positive ions to avoid the need of repeating analyses in two polarities.[25] However, owing to the higher penetration depth and ion-induced mixing, these atomic ion beams could alter the composition of the remaining surfaces and consequently cause artifacts in the dynamic region of the depth profile.[26−28]

An effective approach to minimize these artifacts is utilizing medium-sized polyatomic (such as C$_{60}{}^+$)[29−31] or giant gas cluster (such as Ar$_n{}^+$ and H$_2$O$_n{}^+$)[30−33] ions for the sputter process. While the interaction is more surface localized, these bulky ions with low energy per atom (E/n) induce less significant damage to the remaining surface and lead to less fragmentation of organic species than atomic ions do. With the nonlinearly enhanced sputter rate, they can also remove damage introduced by other beams.[34] In general, although the sputter yield is lower and ion-induced topography may eventually became a problem[35] so that higher E/n (>5−10 eV/atom) was advisible,[36−38] better depth resolution is observed with cluster ions of lower E/n.[39] In other words, depending on the analyte and application, the E/n is to be selected carefully to mitigate analytical artifacts.

For organic−inorganic composite materials, such as hybrid organic metal halide perovskite (ABX$_3$), which consists of organic cations at the A site, metal cations at the B site, and halide anions at the X site, significant preferential sputtering may occur due to different removal rates between the organic and the inorganic components. In fact, while often overlooked, artifacts resulting from the O$_2{}^+$ and Ar-gas cluster ion beam (Ar-GCIB) can be observed in the perovskite depth profiles.[20,21,40] In particular, by comparing the frontside and backside (thermomechanically cleaved at the interface to be the initial surface) depth-profiling results, it was found that the observed composition gradient was an artifact due to damage accumulation when the experimental parameter was not ideal.[25] Thus, strategies for eliminating or alleviating preferential sputtering must be identified before making authentic scientific arguments based on the structure determined with sputter depth profiles. Recently, ToF-SIMS analysis of perovskites and some considerations to mitigate artifacts (such as the use of Bi$_3{}^+$ analysis beam, sputter beams of Ar-GCIB with high E/n, or low-energy atomic O$_2{}^+$ and Cs$^+$, etc.) was reviewed[41] on top of experimental considerations general to ToF-SIMS (such as the use of dual-beam operation with sufficiently high fluence ratio between the sputter and the analysis phase to avoid oversampling, maintaining the signal linearity by constructing the depth profile with lower intensity

SIs that are less likely to arrive within the dead time[42] and saturate the detector, etc.)

In this study, it was identified that the commonly used O_2^+ beam and Ar-GCIB result in preferential intensity loss of the A-site components of methylammonium (MA) and formamidinium (FA) and the extension of Pb and I signals into substrates. These characteristics would lead to incorrect interpretation of the A-site deficiency in the PSC composition and interpenetration at the interface. On the other hand, using either C_{60}^+ or Ar^+ sputter beams, preferential signal loss was eliminated and the resulting depth profile could better reflect the composition for subsequent discussions of how the component distribution was influenced by the deposition procedure. To achieve a high PCE of PSC, it was identified that a uniform component distribution of the perovskite film was essential, and compositional inhomogeneity was found to result in impaired device efficiency and *J*-*V* hysteresis. Regarding the mechanism of device degradation, the results clearly showed halogenation of iodide on the Ag electrode while other components diffused negligibly. These results, obtained by ToF-SIMS with optimization of validated parameters, could serve as guidelines for further development of PSCs.

■ RESULTS AND DISCUSSION

The depth profiles of the $MAPbI_3$ film on the ITO substrate acquired with the commonly used O_2^+ and Ar-GCIB (Ar_{1000}^+, Ar_{4000}^+) sputtering sources are presented in Figure 1. Note that these $MAPbI_3$ films were deposited by the solvent-engineering approach because this method would yield a uniform component distribution[25,36] and could serve as an ideal platform for investigating how sputter ions affect the apparent distribution of components in the resulting depth profile. In addition to the sputter beam that operated in the dynamic region, the acquisition beam could also alter the structure even when the dose was within the static limit. As atomic or small cluster ions, the commonly applied bismuth analysis ions (Bi_x^+, $x = 1-5$) are known to introduce damage to the surface due to their deep penetration depth and artifacts could occur in the resulting depth profiles.[25,43] In particular, while Ar-GCIBs with different E/n were utilized as the sputter beam, similar trends of decreasing intensity of molecular species were observed[25] due to the oversampling, i.e., damage introduced by bismuth ions during the analysis phase cannot be adequately removed in the sputter phase. To avoid oversampling, the relative fluence of bismuth analysis beam and oxygen sputter beam could be lowered to mitigate the associated artifact.[25] However, a lower fluence in the analysis phase would lead to a lower secondary ion intensity (sensitivity), and higher fluence in the sputter phase would lead to a reduced number of data points in the profile (depth resolution). The other possibility to reduce the oversampling is to employ analysis ions that introduce less damage accumulation. For example, as a medium-sized polyatomic cluster, C_{60}^+ can be expected to have more surface-localized interactions and higher sputter yield, so the damage can be suppressed (elaborated below). Therefore, C_{60}^+ was chosen as the acquisition beam in this work.

Damage Accumulation and Preferential Loss of Organic Ion Intensity with O_2^+ Beam. With the commonly used O_2^+ sputtering (Figure 1a−c), it was found that the MA signal decayed rapidly upon exposure to the ion beam. If this result is interpreted directly without consideration of

experimental artifacts, it would suggest a surface-localized MA distribution; hence, the signal intensity of MA is significantly lower in the subsurface. This apparent vertical inhomogeneity might be expected for sequential deposition that converted the deposited PbI_2 film into $MAPbI_3$ during MAI solution soaking, and the limited diffusion kinetics of MAI might explain the surface abundance of MA.[12] The solvent-engineering method used here, however, consisted of a procedure that randomly precipitated precursors on the surface; hence, it was expected to produce uniform MAI-PbI_2-DMSO films that subsequently converted to $MAPbI_3$ with a homogeneous component distribution.[2] Furthermore, the rapidly decayed MA signal was not observed in the profiles acquired using Ar-GCIB sputtering (Figure 1d−i, discussed below). In other words, although it might be an interesting feature for researchers in device physics, the rapidly decayed MA signals observed with O_2^+ sputtering misrepresent the actual distribution of MA and should be ascribed to artifacts; hence, scientific arguments should not be made based on results acquired from O_2^+ directly without validation.

Although the O_2^+ ion is known to enhance ionization yield through surface passivation[44] or oxidation,[22] the rapid oxidation and fragmentation of the MA molecule induced by atomic O_2^+ ion bombardment would also alter its molecular structure; hence, the characteristic signal corresponding to the MA molecule might be lost. As illustrated in Figure S1 (Supporting Information), when the investigated film was irradiated by the sputter beam, surface molecules were simultaneously altered (damaged) and removed. If the damage introduced during either the sputter or the analysis phase cannot be removed by the selected sputter parameter, a damage layer would accumulate,[25,45] and spectra obtained from the information depth in the subsequent analysis phase would be contaminated by the altered molecular structure. In principle, the degree of damage accumulation would reach a steady state with lower signal intensity after a certain ion dose as a result of equilibrium between damaging and removing processes. Occasionally, surface damage was deliberately created to enhance the ionization yield;[22,23,44] however, suitable removal of the damaged layer has always been necessary to avoid artifacts when probing the depth profile.

According to Figure 1a−c, increasing the acceleration voltage of the O_2^+ sputter beam was beneficial to preserve the MA signal, and the bar chart (Figure 2, numerical values are listed in Table S1 of the Supporting Information) clearly shows the tendency of decreasing surface damage with increasing acceleration voltage (higher $I_{MA-steady}/I_{MA-initial}$ value). Similar enhancement in signal preservation with higher O_2^+ beam energy was also reported before.[40] Although a higher beam energy often introduces more damage to the remaining surface and introduces beam-damage artifacts,[25,40,43] these results could be rationalized by the higher sputter rate of higher energy O_2^+ sputtering that removed the damage in a higher rate than at lower voltages; hence, the damage accumulated to a less degree and was better masked. However, even though the sputter rate was up to 45 nm·min^{-1}, a >50% drop in the MA signal intensity was still observed in the profile acquired using O_2^+ sputtering, implying that depth profile artifacts caused by rapid MA oxidation were inevitable with O_2^+ sputtering.

In addition to $MAPbI_3$, a homogeneous $FA_{0.83}Cs_{0.17}PbI_{2.7}Br_{0.3}$ (abbreviated as $FACsPbX_3$) film deposited via the solvent-engineering method was also profiled using
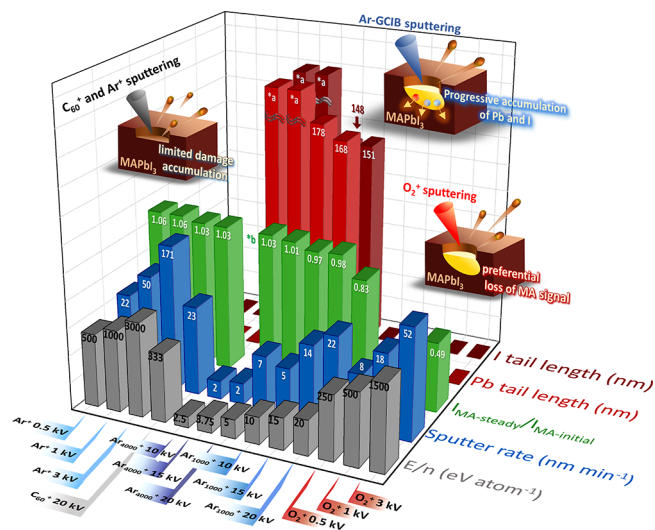
Figure 2. Bar chart summarizing the sputtering parameters and characteristics of the depth profiles. Numerical values are given in Table S1 of the Supporting Information. Height of E/n and sputter rate are expressed on a log scale. *a indicates an infinite tail length. *b indicates a constantly decreasing I_{MA}.

O_2^+ sputtering, and the result is presented in Figure S2. Similar to that of the MA profile, the FA signal also dropped significantly upon exposure to the O_2^+ sputter beam and almost disappeared when reaching the steady state. These results suggested that with O_2^+ sputtering, serious preferential intensity loss of the organic component at the A site would occur due to the preferential sputtering, rapid oxidation, and

fragmentation. Therefore, the acquired depth profile cannot reflect the actual component distribution, negating any subsequent discussion.

Progressive Accumulation of Pb and I and Signal Mixing Induced by Ar-GCIB. With the Ar-GCIBs that are expected to preserve organic species in the sputter depth profiling,[22,37] Figure 1d—i shows that the intensities of the MA, Pb, and I could be better maintained using either Ar_{1000}^+ or Ar_{4000}^+ with acceleration voltages ranging from 10 to 20 kV. While slightly decreased MA signal intensity was observed here with MAPbI$_3$ at 20 eV·atom^{-1} (Figure 1d), pervious work[36] showed improved preservation of FA intensity on $Cs_x(MA_{0.17}FA_{0.83})_{1-x}Pb(I_{0.83}Br_{0.17})_3$ when the E/n was further increased to 40 eV·atom^{-1}. However, it should be noted that the sputter process is highly material dependent. For example, with an identical experimental parameter of 1 kV O_2^+ sputter, Figure 1b and Figure S2 exhibit a significantly different trend of preserving MA and FA signals on MAPbI$_3$ and FACsPbX$_3$, respectively. A similar difference was also observed on MAPbI$_3$ and FAPbI$_3$ using 0.6 kV O_2^+.[40] Furthermore, when the E/n is higher than a cluster- and material-dependent threshold, rapid gelization of organic species may occur.[37] In other words, while GCIB is a promising tool for analyzing organic-containing specimens, E/n needs to be selected carefully.

Upon carefully examining the MAPbI$_3$—ITO interface (insets of respective figures), the appearance of tails in the Pb and I traces when the E/n of Ar-GCIB was below 10 eV·atom^{-1} could not be neglected. The extension of the Pb and I tails, defined as the equivalent perovskite depth between 80% of In and 20% of Pb or I intensities, is summarized in Figure 2 and Table S1. When E/n of the Ar-GCIB was below a
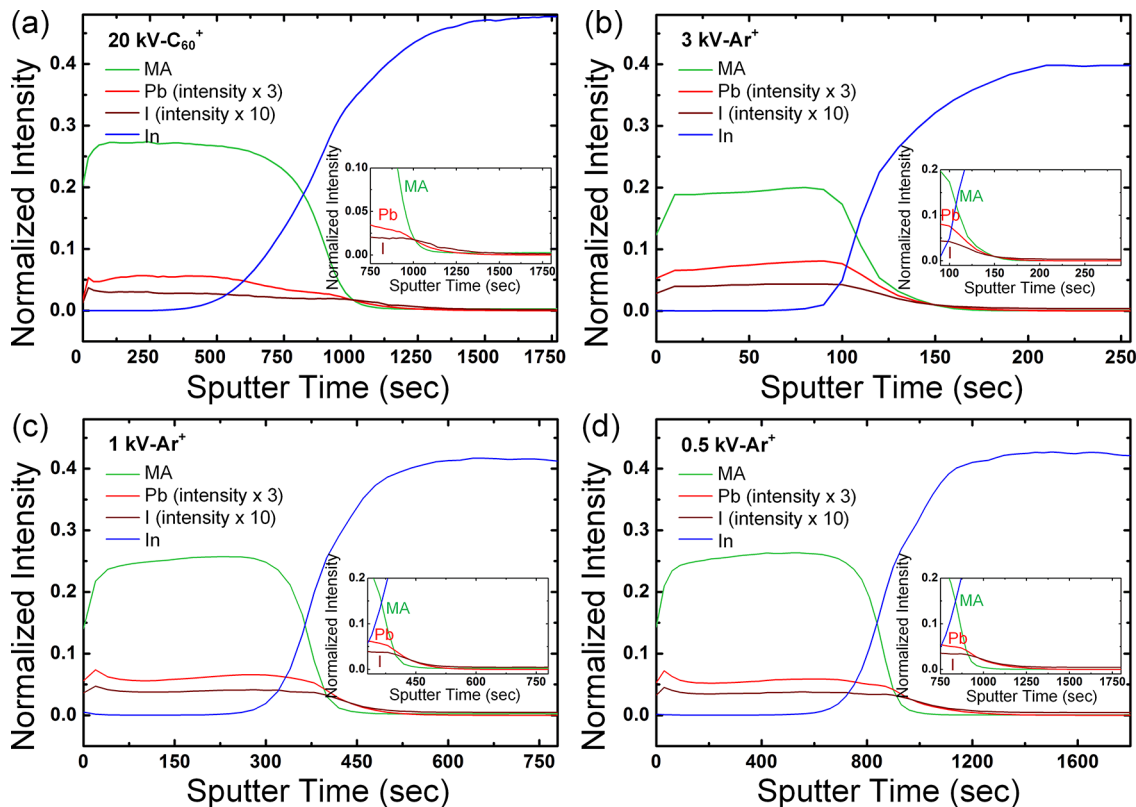
Figure 3. ToF-SIMS depth profiles (normalized with respect to the total ion count of each acquisition) of a solvent-engineered MAPbI$_3$ film on the ITO substrate acquired using (a) 20 kV C_{60}^+ and (b) 3, (c) 1, and (d) 0.5 kV Ar$^+$ sputtering.
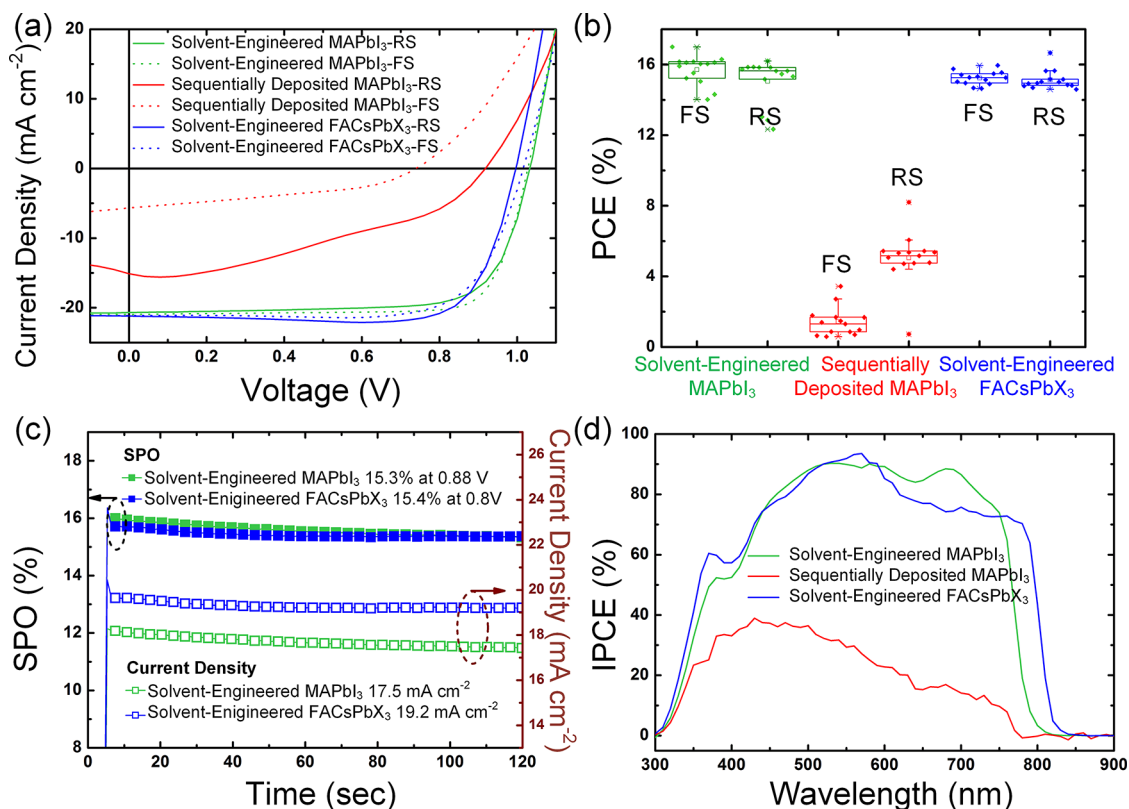
Figure 4. (a) $J-V$ curves (solid lines, reverse scan; dash lines, forward scan) and (b) box plots of PCE values obtained from PSCs utilizing solvent-engineered MAPbI$_3$, sequentially deposited MAPbI$_3$, and solvent-engineered FA$_{0.83}$Cs$_{0.17}$PbI$_{2.7}$Br$_{0.3}$ (FACsPbX$_3$) films as the light-harvesting layer. J_{sc}, V_{oc}, F,F and PCE values are given in Table S2 of the Supporting Information. (c) Steady-state power output (SPO) of solvent-engineered MAPbI$_3$ and solvent-engineered FACsPbX$_3$ devices obtained at the maximum power point. (d) IPCE spectrum of solvent-engineered MAPbI$_3$, sequentially deposited MAPbI$_3$, and solvent-engineered FACsPbX$_3$ devices.

threshold value, the Ar-GCIB had a strong preference for removing organic components, leaving inorganic components behind on the surface.[36,46,47] This preferential loss of organic MA signal and progressive accumulation of inorganic Pb and I originating from the low E/n[36] might explain the observed Pb and I tails mixed with the In signal from the substrate. Although a slight decrease in the MA signal was observed, no Pb or I tail could be identified in profiles acquired using 20 kV Ar$_{1000}^+$ (E/n of 20 eV·atom^{-1}, Figure 1d) and 15 kV Ar$_{1000}^+$ (E/n of 15 eV·atom^{-1}, Figure 1e). When lowering the E/n to 10 eV·atom^{-1} (10 kV Ar$_{1000}^+$, Figure 1f), 168 and 151 nm tails were observed for Pb and I, respectively. Accordingly, a threshold E/n between 10 and 15 eV·atom^{-1} was identified for perovskites. When 20 kV Ar$_{4000}^+$ sputtering (E/n of 5 eV·atom^{-1}, Figure 1g) was applied, the MA signal was well preserved. However, misleading Pb and I tails of 178 and 148 nm, respectively, were observed because the E/n was below the threshold. When E/n was further decreased to below 3.75 eV·atom^{-1} (15 and 10 kV Ar$_{4000}^+$, Figure 1h and 1i, respectively), the signal intensities of the inorganic components dropped very slowly and eventually became constant, independent of sputter time, making the tail length undefinable (marked with *a in Figure 2). This result revealed that Ar-GCIB of low E/n introduced serious mixing of Pb, I, and In signals at the MAPbI$_3$ and ITO interface. Therefore, without careful validation of experimental parameters, such as that presented here, extension of the Pb and I tails into the ITO layer could be mistakenly interpreted as the penetration of PbI$_x$ into ITO or interdiffusion of components. In summary, although Ar-GCIBs could produce depth profiles containing fewer artifacts than in those obtained with O$_2^+$ beams, they may still be inadequate for revealing the true component distribution of MAPbI$_3$ films, especially for those with E/n values lower than 10 eV·atom^{-1}. To obtain profiles with reduced artifact, a higher E/n of 40 eV·atom^{-1} could be used[36] given rapid gelization[37] did not occur. However, the sputter process is highly material dependent; hence, the experimental parameters should be validated for each material.

Properly Identified Component Distributions Acquired by C$_{60}^+$ and Ar$^+$ Beams. Since atomic O$_2^+$ and the giant Ar$_{1000-4000}^+$ cluster ions could not adequately reveal the composition within perovskite and its interface in depth profiles, polyatomic C$_{60}^+$ and nonreactive Ar$^+$ ions were utilized. Using 20 kV C$_{60}^+$ (E/n of 333 eV·atom^{-1}, Figure 3a), the MA signal was found to be well preserved and unlike that observed with Ar-GCIBs, the Pb and I signals did not infiltrate into the ITO layer. This result implied that damage induced by C$_{60}^+$ sputtering could be ignored and justified the use of C$_{60}^+$ as the PI in the acquisition phase. Figure 3b−d shows depth profiles acquired using 3−0.5 kV Ar$^+$ sputtering. Unlike O$_2^+$, Ar$^+$ is chemically inert; hence, MA oxidation could be avoided by implementing Ar$^+$ sputtering. However, high-energy (3 kV) Ar$^+$ sputtering might still introduce damage to the surface, and a lower MA signal was observed in Figure 3b comparing those acquired by its lower energy counterparts. With 1 kV Ar$^+$ sputtering (Figure 3c), other than the shorter analysis time, the resulting depth profile was very similar to that obtained with 20 kV C$_{60}^+$. Further lowering the acceleration voltage to 0.5 kV

([Figure 3](#)d) could not suppress the damage but led to a lower sputter rate, similar to that reported before.[36] 1 kV Ar⁺ sputtering was thus validated to be an adequate parameter for examining the distribution of components in MAPbI₃. To examine whether the 1 kV Ar⁺ could also produce adequate depth profiles of more complicated perovskites, a homogeneous FACsPbX₃ film was profiled. The result shown in [Figure S3](#) confirmed that the depth profile contained negligible artifacts, affirming that the same experimental parameters can be applied to other perovskites for structural analysis, broadening its applicability.

Despite the success presented herein, it is noted that the previously reported $Cs_x(MA_{0.17}FA_{0.83})_{1-x}Pb(I_{0.83}Br_{0.17})_3$ depth profile, acquired using 25 kV Bi_3^+ analysis beam and 1 kV Ar⁺ sputter beam,[36] showed decreased intensities of PbI_3^-, I_2^-, and FAI_2^-, while MAI_3^-, CN^-, and Br^- had a less significant loss of intensity compared to their respective initial intensities before sputtering. In addition to the material-dependent sputter process and damage accumulation, the difference may also be rationalized by considering the ions selected for generating the depth profile. While compound ions allow analysis of both electropositive and electronegative components in a single polarity of secondary ions and their lower intensities effectively avoid the nonlinearity due to saturation of the detector,[41] the higher damage cross-section of compound ions might lead to more significant damage accumulation and artifacts in the depth profile. In the presenting work, since compound ions were not used and the linearity of secondary ion intensities[42] was maintained by C_{60}^+ analysis beam of low current and pulse length, perovskites were successfully profiled with 1 kV Ar⁺ sputter.

Performance Difference between PSCs Fabricated by Different Methods. To prepare a well-controlled perovskite film to achieve a highly efficient PSC, a number of procedures were proposed.[2,48−50] However, it was noted that a wide range of variations have been reported regarding PSC efficiency, which is usually ascribed to the difference in film quality, and yet, a clear and perhaps unified explanation is still lacking. Because of the lack of suitable analytical tools that could obtain the actual component distribution inside perovskite films, the relationship between the component distribution and the device performance has rarely been discussed. On the basis of the validated analysis of the component distribution inside perovskite films demonstrated in this study, the capability to investigate the influence of fabrication processes on the resulting structure and the corresponding device performance was demonstrated. [Figure 4](#) shows the device performance of PSCs utilizing the same device architecture of ITO/NiO/perovskite/PCBM/polyethylenimine(PEI)/Ag but different methods in preparing the perovskite layer. The comparison was made among popular fabrication methods, including (1) solvent engineering,[2] which utilizes an antisolvent dispersion step during the spin-coating process to precipitate precursor films, and (2) sequential deposition,[49] which involves predeposition of the PbI_2 film and subsequent conversion of the PbI_2 film into MAPbI₃. In addition to MAPbI₃, a device using FACsPbX₃, a perovskite with a lower bandgap than that of MAPbI₃,[7] was also prepared for comparison.

For MAPbI₃ devices, [Figure 4](#) (numerical values are summarized in [Table S2](#) of the Supporting Information) shows that solvent engineering yielded better device performance than sequential deposition. In addition to the increased PCE from 5.1% to 15.1%, the $J-V$ hysteresis between the forward scan (FS) and the reverse scan (RS) was also eliminated. Statistical PCE box plots and the steady-state power output (SPO) measurements, shown in [Figure 4](#)b and [4](#)c, respectively, also indicated a higher PCE and less $J-V$ hysteresis of the solvent-engineering device than that of the sequential deposition device. Other than a higher PCE, solvent engineering also enabled well-controlled fabrication of more complicated perov-

skites,[6,8,9,21] such as FACsPbX₃. Compared with those of the MAPbI₃ device, the FACsPbX₃ device had a higher J_{sc} and a lower V_{oc} due to its smaller band gap, which was confirmed by the extended response range of 800−830 nm in the incident photon-to-electron conversion efficiency (IPCE) spectrum shown in [Figure 4](#)d.

Despite the remarkable performance difference between the solvent-engineered and the sequentially deposited MAPbI₃ devices, little difference in surface morphology ([Figure S4](#)) and X-ray diffraction (XRD, [Figure S5](#)) could be identified. In terms of morphology, both solvent engineering and sequential deposition yielded close-packed MAPbI₃ crystals with a crystal size of hundreds of nanometers. For the crystalline structure, the XRD patterns were almost identical except for the weak PbI_2 peak acquired from the sequentially deposited MAPbI₃ film, indicating incomplete conversion of the PbI_2 film. Since many groups have demonstrated highly efficient PSCs with an excess of the PbI_2 phase in the perovskite layer,[12,13] the PbI_2 phase observed here could not explain its poor performance. Thus, there must have been other governing factors that determined whether the PbI_2 phase would lower the device performance. While XRD provided averaged structural information across the analysis volume, a depth-resolved analysis might provide insight into the device performance.

Film-Formation Mechanisms of Perovskite Films Fabricated by Different Methods. [Figure 5](#)a shows the comparison of depth profiles between the solvent-engineered and the sequentially deposited MAPbI₃ films, both of which were deposited on the NiO hole-transporting layer (HTL) to examine the spatial distribution of components. While the solvent-engineered MAPbI₃ film showed uniform MA and Pb profiles, a significant MA deficiency was found in
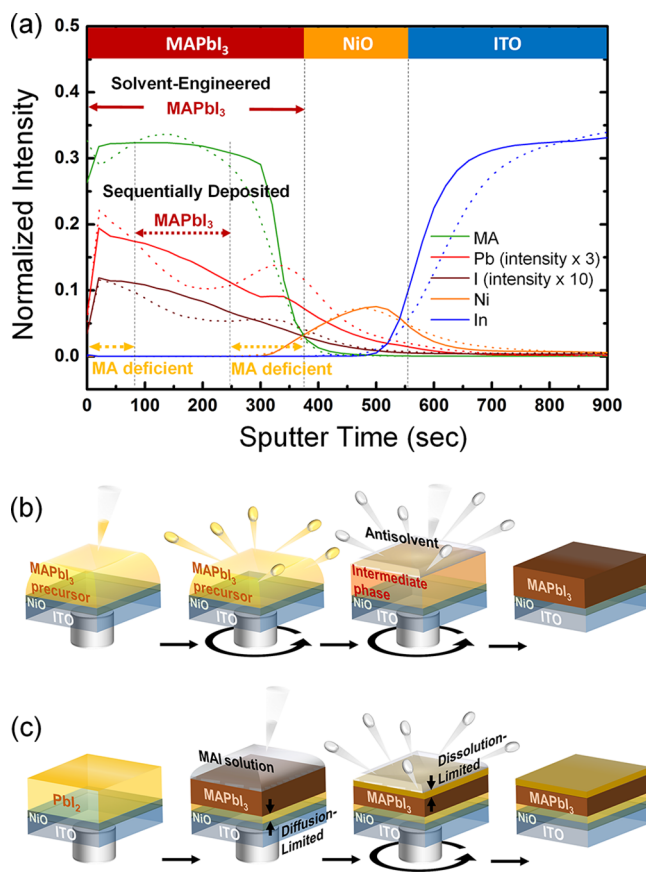
Figure 5. (a) Depth profiles of an MAPbI₃ film (solid lines. solvent-engineered; dash lines, sequentially deposited) on the NiO/ITO substrate acquired with 1 kV Ar⁺ sputter. Schematic illustration of the film-formation mechanism during the (b) solvent-engineering and (c) sequential deposition processes.

the top and bottom layers in the sequentially deposited MAPbI₃ film. These distinctive features could be rationalized by film-formation mechanisms illustrated in Figure 5b and 5c. During solvent-engineering deposition, formation of the intermediate phase occurred immediately when the antisolvent was dispersed on the substrate.[2] This intermediate phase was then converted into perovskite crystals by subsequent annealing. The rapid precipitation yielded randomly and homogeneously distributed precursor films, which greatly limited the diffusion kinetics. As a result, the resultant solvent-engineered MAPbI₃ film possessed a uniform component distribution. For a more complicated solvent-engineered FACsPbX₃ film (Figure S3), a uniform distribution of the FA, Cs, Pb, I, and Br components could also be identified, supporting the proposed film-formation mechanism. On the other hand, for the sequential deposition process, a PbI₂ film was first deposited on the substrate before MAI solution soaking, which converted the PbI₂ film into MAPbI₃ crystals. Due to the limited diffusion of MAI inside PbI₂, the PbI₂ at the bottom might not be completely converted and a diffusion-limited layer, as illustrated in Figure 5c, remained. The soaking process was followed by a spinning step that removed excess MAI solution. During this spinning process, the vigorous flow of the polar solvent partially dissolved nascent MAPbI₃ crystals and MAI, resulting in an MA-deficient layer on the top surface, as illustrated in Figure 5c as a dissolution-limited layer. In the end, the sequentially deposited MAPbI₃ film consisted of a MAPbI₃ layer sandwiched between MA-deficient layers. These MA-deficient layers severely hinder the device performance due to the decreased carrier lifetime and the impaired transport dynamics.[12,13] As a result, the sequentially deposited device showed lower performance than that of the solvent-engineered device in every metric. Although the MA-deficient (PbI₂) phase was reported to passivate defects at the interface and grain boundaries,[12,13,51] an MA-deficient layer should be avoided according to the aforementioned discussion. These results indicate that controlling the distribution of the MA-deficient phase plays an essential role in the further development of PSCs.

Degradation Mechanisms of PSCs. In terms of device degradation mechanisms, the depth profiles of fresh and 7 day aged PSCs fabricated with solvent-engineered MAPbI₃ were compared to examine the possible change in component distribution inside the PSC. In Figure 6a, the PCBM had a relatively wide distribution and infiltrated into the MAPbI₃ layer because of the rugged interface and the polycrystalline nature of the MAPbI₃ film. The spike of the Ag peak at the Ag/PCBM interface was attributed to the enhanced ionization yield of Ag⁺ due to electron-withdrawing PCBM in the vicinity, which is known as the matrix effect in SIMS analysis. For the 7 day old device, the MA profile remained unchanged, which was contrary to the expected MA diffusion and formation of the MA-deficient phase.[52,53] This observation suggested that the migration or escape of MA was not the dominant factor during the degradation process at room temperature.

According to Figure 6b, halogenation of the Ag electrode was the main characteristic that appeared after aging. This observation indicated that iodide diffusion was the main cause of PCE degradation[54] and J−V hysteresis, as shown in Figure 6c. For the occurrence of iodide diffusion, MAPbI₃ must be decomposed so that the iodide ions become mobile. Such decomposition could be accelerated by environmental stimulations such as thermal stress,[52,53] moisture attack,[55] and light soaking.[56,57] The degradation mechanism identified here that consists of iodide diffusion may provide grounds for further enhancing the stability of PSCs through the development of a more stable perovskite configuration.

■ CONCLUSIONS

The most commonly applied O₂⁺ and Ar-GCIB sputtering methods generated artifacts in the depth profile of perovskite
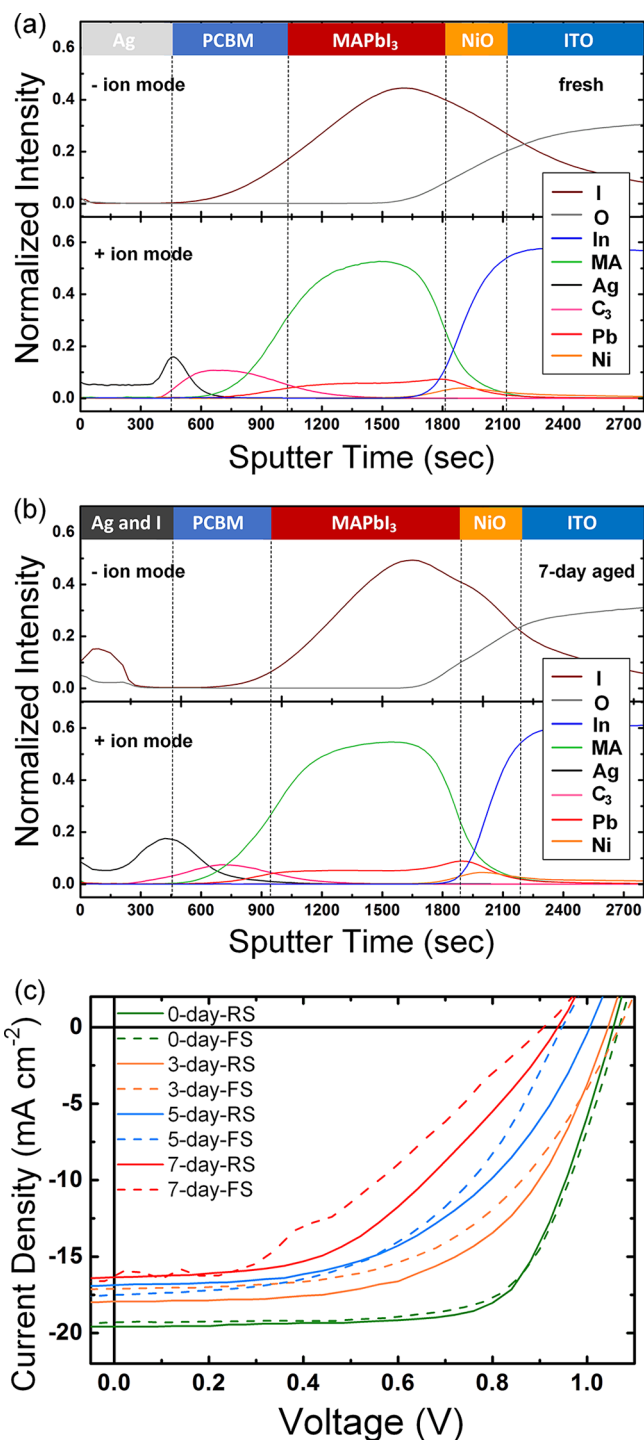
Figure 6. Depth profiles (acquired with 1 kV Ar⁺ sputter) of (a) fresh and (b) 7 day aged MAPbI₃ devices fabricated with solvent engineering. (c) J−V curves (solid lines, reverse scan; dashed lines, forward scan) of MAPbI₃ devices after 0, 3, 5, and 7 days of aging.

films due to the preferential intensity loss of the A-site components and the induced mixing of Pb and I signals with the ITO substrates. By utilizing C₆₀⁺ or Ar⁺ sputtering, artifacts could be eliminated, and the distribution of components inside PSCs could be more properly determined. In terms of the effect of the fabrication process, it was found that the distribution of the MA-deficient (or residual PbI₂) layer inside the perovskite film was a governing factor for its performance. On one hand, solvent-engineered perovskite films possessed a

uniform component distribution and yielded high efficiency. On the other hand, perovskite films fabricated by sequential deposition were sandwiched by MA-deficient layers that led to a lower PCE than that of the solvent-engineered film and significant $J-V$ hysteresis. In terms of the degradation mechanism, diffusion of iodide was the main feature that appeared after aging. These results are essential for the development of more efficient and stable PSCs. More importantly, using PSC as the example, choosing proper sputter parameters for the sputter depth profile was proven to be crucial for obtaining valid information. This concept is also applicable to other surface analysis techniques, such as X-ray photoelectron spectroscopy (XPS) and Auger electron spectroscopy (AES), which are utilized to probe the thin-film material. For ion sputter-based analytical techniques, reference specimens should always be used to ensure that the observed compositional differences are not artifacts caused by the sputtering process. This is an essential process for correctly identifying the performance and degradation mechanism in thin-film devices.

■ METHODS

Chemicals. All chemical compounds utilized in this study were commercially available and used as received, including nickel 2-ethylhexanoate (78% in ethylhexanoic acid, Sigma-Aldrich), MAI (low water content, TCI), FAI (low water content, TCI), PbI_2 (99.99%, TCI), $PbBr_2$ (98%, TCI), CsI (99.999%, Alfa Aesar), [6,6]-phenyl-C61-butyric acid methyl ester ($PC_{61}BM$, >99%, Solenne), and branched polyethylenimine (PEI, M_w 25 000, Sigma-Aldrich). Solvents, including N,N-dimethylformamide (DMF), dimethyl sulfoxide (DMSO), diethyl ether, chlorobenzene (CB), ethanol, and isopropanol, were anhydrous and purchased from Sigma-Aldrich.

Thin Film and Device Fabrication. The solvent-engineering[2] and sequential deposition[49] methods were utilized to deposit the perovskite film inside a glovebox with N_2 atmosphere (O_2 and H_2O < 1 ppm). For solvent engineering, the perovskite layer was spin coated from a solution with a mixed solvent (DMF:DMSO = 4:1, v:v) and 1.33 M perovskite precursors. After 5 s of 1000 rpm spinning, the rotation rate was increased to 3500 rpm and maintained for another 30 s. During the last 12 s, antisolvent (diethyl ether) was gently dispensed and a compact layer with the intermediate phase was formed. For the $MAPbI_3$ film, the substrate was then annealed on a 50 °C hot plate for 2 min, followed by another 2 min on a 100 °C hot plate. For the $FA_{0.83}Cs_{0.17}PbI_{2.7}Br_{0.3}$ (abbreviated as $FACsPbX_3$) film, the substrate was annealed on a 100 °C hot plate for 1 h. In sequential deposition, a PbI_2 layer was spin coated from a PbI_2 solution (1.0 M in DMF) at 4000 rpm for 60 s and followed by a 30 min annealing at 70 °C on a hot plate. The MAI solution (0.2 M in isopropanol) was poured on the substrate to convert PbI_2 into $MAPbI_3$. After 20 s of soaking, the substrate was rotated at 4000 rpm for 30 s before it was annealed at 100 °C on a hot plate for 1 h.

The PSC fabricated here had a device architecture of ITO/NiO/perovskite/PCBM/PEI/Ag. To complete the device, the ITO glass substrate (10 $\Omega\cdot\square^{-1}$) was ultrasonically cleaned sequentially in a deionized water, acetone, and isopropanol bath. The NiO precursor was then spin coated from the 0.3 M nickel 2-ethylhexanoate solution in ethanol at 1400 rpm for 60 s inside of a glovebox. The substrate was then annealed in air at 280 °C for 1 h. After that, the substrate was transferred back into the glovebox, and a perovskite layer was deposited on the NiO hole-transporting layer (HTL) via the above-described procedure. The PCBM electron-transporting layer (ETL) was then spin coated from a CB solution of 20 mg·mL^{-1} at 1000 rpm for 30 s. Before the 100 nm Ag electrode was deposited via thermal evaporation, a PEI work-function modifier was spin coated from an isopropanol solution of 0.1 wt % at 3500 rpm for 30 s.

ToF-SIMS Depth Profiling. All time-of-flight secondary-ion mass spectrometry (ToF-SIMS) depth profiles were acquired with a PHI TRIFT V nanoTOF (ULVAC-PHI, Japan) using a dual-beam slice-and-view scheme. During the analysis phase, a pulsed C_{60}^+ (approximately 8200 Hz, 15 ns pulse length) was used as the primary ion. The acceleration voltage of the C_{60}^+ was 20 kV, and the beam current was 0.15 nA-DC. A spectrum in each analysis phase was acquired by rastering the C_{60}^+ beam over a 50 μm × 50 μm area with an incident angle of 42°. The acquisition time was 3 min, yielding a total primary ion dosage of 8.3 × 10^{11} ions·cm^{-2} in each analysis, which was below the static limit of 1.0 × 10^{12} ions·cm^{-2}. Secondary ions were accelerated by a pulsed 3 kV sample bias and traveled 2 m before reaching the detector. During the analysis, pulsed 10 V electron and 10 V ion flooding were applied to compensate for the surface charge. The intensity of ions in each analysis cycle was normalized by the respective total ion intensity to compensate for possible fluctuations of the primary ion current. In the sputter phase, different acceleration voltages of O_2^+, Ar^+, C_{60}^+, Ar_{4000}^+, and Ar_{1000}^+ were applied to etch the surface. For O_2^+ and Ar^+ sputtering, the acceleration voltage (0.5−3 kV) was adjusted using a 500−0 V floating column (model 06-350, ULVAC-PHI, Japan) with an incident angle of 45°. A floating voltage of 500 V was applied to decelerate the 1 kV ions for the 0.5 kV sputtering, and 0 V floating was applied for the 1 and 3 kV sputtering. The current density adjusted by the strength of the condenser lens was 17.8 μA/cm^2 (400 nA over a 1500 μm × 1500 μm area), and the sputter interval was between 10 and 30 s. For C_{60}^+ sputtering, the acceleration voltage was 20 kV and the current density was 0.4 μA/cm^2 (1 nA over a 500 μm × 500 μm area). The incident angle was 42°, and the sputter interval was 20 s. For Ar_{4000}^+ and Ar_{1000}^+ sputtering, Wein-filtered Ar-GCIB (model 06-2100, ULVAC-PHI, Japan) was used to generate Ar_{4000}^+ and Ar_{1000}^+ cluster ions with different kinetic energies (10, 15, and 20 keV). The cluster size was controlled by the Ar pressure, and the relationship between the Ar pressure and the cluster size was provided by the manufacturer. The currents of the Ar_{4000}^+ and Ar_{1000}^+ beams were both fine tuned to 1.6 μA/cm^2 (4 nA over a 500 μm × 500 μm area). The incident angle was 50°, and the sputter interval was 120 s.

Characterization. The $J-V$ characteristic of a PSC was collected using a Keithley 2400 source meter with a voltage step of 10 mV and a 50 ms dwell time, while the device was illuminated by a standard air mass 1.5 sunlight generated by a solar simulator (model 69920, Newport) with an integrated intensity of 100 mW cm^{-2} calibrated by a reference cell (model 91150-KG5, Newport) before each measurement. The voltage of the forward sweep (FS) curve was from −0.1 to 1.2 V, and the reverse sweep (RS) curve was from 1.2 to −0.1 V. The active area of the PSC device was 0.09 cm^2 as defined by the area of the Ag electrode. For steady-state power output (SPO) measurements, the photocurrent was constantly recorded while the device was operated at the bias that yielded the maximum power conversion efficiency (PCE) value during the $J-V$ scan. For incident photon−electron conversion efficiency (IPCE) measurements, the device was illuminated by a monochromatic beam generated by a 300 W Xe lamp (model 6258, Newport Oriel) and a monochromator (model 74100, Oriel). The intensity of the monochromatic beam was calibrated by a power meter (model 1936-C, Newport) equipped with a photodetector (model 818-UV, Newport). During the aging test, the unencapsulated PSCs were stored in a dark, room-temperature environment with a relative humidity of 50−60%. The SEM images were acquired using a field-emission Nova200 NanoSEM system (FEI, USA) or PHI690 Auger Nanoprobe (ULVAC-PHI, Japan) without conductive overcoat. The XRD patterns were acquired with a TTRAX3 X-ray diffractometer (Rigaku, Japan) using a Cu Kα beam.

■ ASSOCIATED CONTENT

ⓈI Supporting Information

The Supporting Information is available free of charge at https://pubs.acs.org/doi/10.1021/acsami.9b22492.

Illustration of ToF-SIMS depth profiling, ToF-SIMS depth profiles of $FACsPbX_3$, SEM and XRD results of

MAPbI$_3$, table summarizing numerical values of Figure 2, and table summarizing the PSC metrics (PDF)

■ AUTHOR INFORMATION

Corresponding Author

    Jing-Jong Shyue − *Research Center for Applied Sciences, Academia Sinica, Taipei 11529, Taiwan; Department of Materials Science and Engineering, National Taiwan University, Taipei 10617, Taiwan;* ◉ orcid.org/0000-0002-8508-659X; Email: shyue@gate.sinica.edu.tw

Authors

    Cheng-Hung Hou − *Research Center for Applied Sciences, Academia Sinica, Taipei 11529, Taiwan;* ◉ orcid.org/0000-0002-5150-7106

    Shu-Han Hung − *Research Center for Applied Sciences, Academia Sinica, Taipei 11529, Taiwan*

    Li-Ji Jhang − *Research Center for Applied Sciences, Academia Sinica, Taipei 11529, Taiwan*

    Keh-Jiunh Chou − *Department of Chemistry, National Taiwan University, Taipei 10617, Taiwan*

    Yu-Kai Hu − *Department of Chemistry, National Taiwan University, Taipei 10617, Taiwan*

    Pi-Tai Chou − *Department of Chemistry, National Taiwan University, Taipei 10617, Taiwan;* ◉ orcid.org/0000-0002-8925-7747

    Wei-Fang Su − *Department of Materials Science and Engineering, National Taiwan University, Taipei 10617, Taiwan;* ◉ orcid.org/0000-0002-3375-4664

    Feng-Yu Tsai − *Department of Materials Science and Engineering, National Taiwan University, Taipei 10617, Taiwan;* ◉ orcid.org/0000-0003-4664-2706

    Jay Shieh − *Department of Materials Science and Engineering, National Taiwan University, Taipei 10617, Taiwan;* ◉ orcid.org/0000-0002-0979-8288

Complete contact information is available at:
https://pubs.acs.org/10.1021/acsami.9b22492

Author Contributions

C.H.H. and J.J.S. conceived the experiments and led the project. C.H.H., S.H.H., L.J.J., and J.J.S. conducted the ToF-SIMS depth profiling and SEM measurements. K.J.C., Y.K.H., and P.T.C. performed the PCE, SPO, IPCE, and XRD characterizations. C.H.H., W.F.S., F.Y.T., and J.S. were responsible for PSC fabrication and the aging test. C.H.H. and J.J.S. wrote the manuscript with contributions from all authors.

Notes

The authors declare no competing financial interest.

■ REFERENCES

(1) Lee, M. M.; Teuscher, J.; Miyasaka, T.; Murakami, T. N.; Snaith, H. J. Efficient Hybrid Solar Cells Based on Meso-Superstructured Organometal Halide Perovskites. *Science* **2012**, *338* (6107), 643−647.

(2) Jeon, N. J.; Noh, J. H.; Kim, Y. C.; Yang, W. S.; Ryu, S.; Seok, S. I. Solvent Engineering for High-Performance Inorganic−Organic Hybrid Perovskite Solar Cells. *Nat. Mater.* **2014**, *13* (9), 897.

(3) Yang, W. S.; Park, B.-W.; Jung, E. H.; Jeon, N. J.; Kim, Y. C.; Lee, D. U.; Shin, S. S.; Seo, J.; Kim, E. K.; Noh, J. H.; et al. Iodide Management in Formamidinium-Lead-Halide−Based Perovskite Layers for Efficient Solar Cells. *Science* **2017**, *356* (6345), 1376−1379.

(4) He, M.; Li, B.; Cui, X.; Jiang, B.; He, Y.; Chen, Y.; O'Neil, D.; Szymanski, P.; Ei-Sayed, M. A.; Huang, J.; et al. Meniscus-Assisted Solution Printing of Large-Grained Perovskite Films for High-Efficiency Solar Cells. *Nat. Commun.* **2017**, *8*, 16045.

(5) Deng, Y.; Peng, E.; Shao, Y.; Xiao, Z.; Dong, Q.; Huang, J. Scalable Fabrication of Efficient Organolead Trihalide Perovskite Solar Cells with Doctor-Bladed Active Layers. *Energy Environ. Sci.* **2015**, *8* (5), 1544−1550.

(6) Jeon, N. J.; Noh, J. H.; Yang, W. S.; Kim, Y. C.; Ryu, S.; Seo, J.; Seok, S. I. Compositional Engineering of Perovskite Materials for High-Performance Solar Cells. *Nature* **2015**, *517* (7535), 476.

(7) McMeekin, D. P.; Sadoughi, G.; Rehman, W.; Eperon, G. E.; Saliba, M.; Hörantner, M. T.; Haghighirad, A.; Sakai, N.; Korte, L.; Rech, B.; et al. A Mixed-Cation Lead Mixed-Halide Perovskite Absorber for Tandem Solar Cells. *Science* **2016**, *351* (6269), 151−155.

(8) Jesper Jacobsson, T.; Correa-Baena, J.-P.; Pazoki, M.; Saliba, M.; Schenk, K.; Gratzel, M.; Hagfeldt, A. Exploration of the Compositional Space for Mixed Lead Halogen Perovskites for High Efficiency Solar Cells. *Energy Environ. Sci.* **2016**, *9* (5), 1706−1724.

(9) Bush, K. A.; Palmstrom, A. F.; Yu, Z. J.; Boccard, M.; Cheacharoen, R.; Mailoa, J. P.; McMeekin, D. P.; Hoye, R. L. Z.; Bailie, C. D.; Leijtens, T.; et al. 23.6%-Efficient Monolithic Perovskite/Silicon Tandem Solar Cells with Improved Stability. *Nat. Energy* **2017**, *2* (4), 17009.

(10) Sahli, F.; Werner, J.; Kamino, B. A.; Brauninger, M.; Monnard, R.; Paviet-Salomon, B.; Barraud, L.; Ding, L.; Diaz Leon, J. J.; Sacchetto, D.; et al. Fully Textured Monolithic Perovskite/Silicon Tandem Solar Cells with 25.2% Power Conversion Efficiency. *Nat. Mater.* **2018**, *17* (9), 820.

(11) Leijtens, T.; Bush, K. A.; Prasanna, R.; McGehee, M. D. Opportunities and Challenges for Tandem Solar Cells Using Metal Halide Perovskite Semiconductors. *Nat. Energy* **2018**, *3* (10), 828.

(12) Jacobsson, T. J.; Correa-Baena, J.-P.; Halvani Anaraki, E.; Philippe, B.; Stranks, S. D.; Bouduban, M. E.; Tress, W.; Schenk, K.; Teuscher, J. l.; Moser, J.-E.; et al. Unreacted Pbi2 as a Double-Edged Sword for Enhancing the Performance of Perovskite Solar Cells. *J. Am. Chem. Soc.* **2016**, *138* (32), 10331−10343.

(13) Jiang, Q.; Chu, Z.; Wang, P.; Yang, X.; Liu, H.; Wang, Y.; Yin, Z.; Wu, J.; Zhang, X.; You, J. Planar-Structure Perovskite Solar Cells with Efficiency Beyond 21%. *Adv. Mater.* **2017**, *29* (46), 1703852.

(14) Xiao, Z.; Yuan, Y.; Shao, Y.; Wang, Q.; Dong, Q.; Bi, C.; Sharma, P.; Gruverman, A.; Huang, J. Giant Switchable Photovoltaic Effect in Organometal Trihalide Perovskite Devices. *Nat. Mater.* **2015**, *14* (2), 193.

(15) Eames, C.; Frost, J. M.; Barnes, P. R.; O'regan, B. C.; Walsh, A.; Islam, M. S. Ionic Transport in Hybrid Lead Iodide Perovskite Solar Cells. *Nat. Commun.* **2015**, *6*, 7497.

(16) Matteocci, F.; Busby, Y.; Pireaux, J.-J.; Divitini, G.; Cacovich, S.; Ducati, C.; Di Carlo, A. Interface and Composition Analysis on Perovskite Solar Cells. *ACS Appl. Mater. Interfaces* **2015**, *7* (47), 26176−26183.

(17) Dou, B.; Wheeler, L. M.; Christians, J. A.; Moore, D. T.; Harvey, S. P.; Berry, J. J.; Barnes, F. S.; Shaheen, S. E.; van Hest, M. F. Degradation of Highly Alloyed Metal Halide Perovskite Precursor Inks: Mechanism and Storage Solutions. *ACS Energy Lett.* **2018**, *3* (4), 979−985.

(18) Domanski, K.; Correa-Baena, J.-P.; Mine, N.; Nazeeruddin, M. K.; Abate, A.; Saliba, M.; Tress, W.; Hagfeldt, A.; Grätzel, M. Not All That Glitters Is Gold: Metal-Migration-Induced Degradation in Perovskite Solar Cells. *ACS Nano* **2016**, *10* (6), 6306−6314.

(19) Zhang, T.; Meng, X.; Bai, Y.; Xiao, S.; Hu, C.; Yang, Y.; Chen, H.; Yang, S. Profiling the Organic Cation-Dependent Degradation of Organolead Halide Perovskite Solar Cells. *J. Mater. Chem. A* **2017**, *5* (3), 1103−1111.

(20) Zhao, Y.; Zhou, W.; Tan, H.; Fu, R.; Li, Q.; Lin, F.; Yu, D.; Walters, G.; Sargent, E. H.; Zhao, Q. Mobile-Ion-Induced Degradation of Organic Hole-Selective Layers in Perovskite Solar Cells. *J. Phys. Chem. C* **2017**, *121* (27), 14517−14523.

(21) Christians, J. A.; Schulz, P.; Tinkham, J. S.; Schloemer, T. H.; Harvey, S. P.; Tremolet de Villers, B. J.; Sellinger, A.; Berry, J. J.; Luther, J. M. Tailored Interfaces of Unencapsulated Perovskite Solar Cells for> 1,000 h Operational Stability. *Nat. Energy* **2018**, *3* (1), 68.

(22) Chu, Y.-H.; Liao, H.-Y.; Lin, K.-Y.; Chang, H.-Y.; Kao, W.-L.; Kuo, D.-Y.; You, Y.-W.; Chu, K.-J.; Wu, C.-Y.; Shyue, J.-J. Improvement of the Gas Cluster Ion Beam-(Gcib)-Based Molecular Secondary Ion Mass Spectroscopy (Sims) Depth Profile with O 2+ Cosputtering. *Analyst* **2016**, *141* (8), 2523−2533.

(23) Yu, B.-Y.; Lin, W.-C.; Wang, W.-B.; Iida, S.-i.; Chen, S.-Z.; Liu, C.-Y.; Kuo, C.-H.; Lee, S.-H.; Kao, W.-L.; Yen, G.-J.; et al. Effect of Fabrication Parameters on Three-Dimensional Nanostructures of Bulk Heterojunctions Imaged by High-Resolution Scanning Tof-Sims. *ACS Nano* **2010**, *4* (2), 833−840.

(24) Brison, J.; Hubert, R.; Lucas, S.; Houssiau, L. An Application of Cesium−Xenon Co-Sputtering: Quantitative Study of a Pd−Rh Thin Film by Tof-Sims. *Surf. Interface Anal.* **2006**, *38* (12−13), 1654−1657.

(25) Harvey, S. P.; Zhang, F.; Palmstrom, A.; Luther, J. M.; Zhu, K.; Berry, J. J. Mitigating Measurement Artifacts in Tof-Sims Analysis of Perovskite Solar Cells. *ACS Appl. Mater. Interfaces* **2019**, *11*, 30911−30918.

(26) Mahoney, C. M. Cluster Secondary Ion Mass Spectrometry of Polymers and Related Materials. *Mass Spectrom. Rev.* **2009**, *29* (2), 247−293.

(27) Mahoney, C. M.; Fahey, A. J.; Gillen, G. Temperature-Controlled Depth Profiling of Poly (Methyl Methacrylate) Using Cluster Secondary Ion Mass Spectrometry. 1. Investigation of Depth Profile Characteristics. *Anal. Chem.* **2007**, *79* (3), 828−836.

(28) Mahoney, C. M.; Fahey, A. J.; Gillen, G.; Xu, C.; Batteas, J. D. Temperature-Controlled Depth Profiling of Poly (Methyl Methacrylate) Using Cluster Secondary Ion Mass Spectrometry. 2. Investigation of Sputter-Induced Topography, Chemical Damage, and Depolymerization Effects. *Anal. Chem.* **2007**, *79* (3), 837−845.

(29) Fletcher, J. S.; Conlan, X. A.; Jones, E. A.; Biddulph, G.; Lockyer, N. P.; Vickerman, J. C. Tof-Sims Analysis Using C60. Effect of Impact Energy on Yield and Damage. *Anal. Chem.* **2006**, *78* (6), 1827−1831.

(30) Rabbani, S.; Barber, A. M.; Fletcher, J. S.; Lockyer, N. P.; Vickerman, J. C. Tof-Sims with Argon Gas Cluster Ion Beams: A Comparison with C60+. *Anal. Chem.* **2011**, *83* (10), 3793−3800.

(31) Mouhib, T.; Poleunis, C.; Wehbe, N.; Michels, J.; Galagan, Y.; Houssiau, L.; Bertrand, P.; Delcorte, A. Molecular Depth Profiling of Organic Photovoltaic Heterojunction Layers by Tof-Sims: Comparative Evaluation of Three Sputtering Beams. *Analyst* **2013**, *138* (22), 6801−6810.

(32) Shard, A. G.; Havelund, R.; Seah, M. P.; Spencer, S. J.; Gilmore, I. S.; Winograd, N.; Mao, D.; Miyayama, T.; Niehuis, E.; Rading, D.; et al. Argon Cluster Ion Beams for Organic Depth Profiling: Results from a Vamas Interlaboratory Study. *Anal. Chem.* **2012**, *84* (18), 7865−7873.

(33) Sheraz née Rabbani, S.; Barber, A.; Fletcher, J. S.; Lockyer, N. P.; Vickerman, J. C. Enhancing Secondary Ion Yields in Time of Flight-Secondary Ion Mass Spectrometry Using Water Cluster Primary Beams. *Anal. Chem.* **2013**, *85* (12), 5654−5658.

(34) Miyayama, T.; Sanada, N.; Bryan, S. R.; Hammond, J. S.; Suzuki, M. Removal of Ar+ Beam-Induced Damaged Layers from Polyimide Surfaces with Argon Gas Cluster Ion Beams. *Surf. Interface Anal.* **2010**, *42* (9), 1453−1457.

(35) Niehuis, E.; Mollers, R.; Rading, D.; Cramer, H.-G.; Kersting, R. Analysis of Organic Multilayers and 3d Structures Using Ar Cluster Ions. *Surf. Interface Anal.* **2013**, *45* (1), 158−162.

(36) Noël, C.; Pescetelli, S.; Agresti, A.; Franquet, A.; Spampinato, V.; Felten, A.; di Carlo, A.; Houssiau, L.; Busby, Y. Hybrid Perovskites Depth Profiling with Variable-Size Argon Clusters and Monatomic Ions Beams. *Materials* **2019**, *12*, 726.

(37) Wang, S.-K.; Chang, H.-Y.; Chu, Y.-H.; Kao, W.-L.; Wu, C.-Y.; Lee, Y.-W.; You, Y.-W.; Chu, K.-J.; Hung, S.-H.; Shyue, J.-J. J. A. Effect of Energy Per Atom (E/N) on the Ar Gas Cluster Ion Beam (Ar-Gcib) and O 2+ Cosputter Process. *Analyst* **2019**, *144* (10), 3323−3333.

(38) Shen, K.; Wucher, A.; Winograd, N. Molecular Depth Profiling with Argon Gas Cluster Ion Beams. *J. Phys. Chem. C* **2015**, *119* (27), 15316−15324.

(39) Seah, M.; Spencer, S.; Havelund, R.; Gilmore, I.; Shard, A. J. A. Depth Resolution at Organic Interfaces Sputtered by Argon Gas Cluster Ions: The Effect of Energy, Angle and Cluster Size. *Analyst* **2015**, *140* (19), 6508−6516.

(40) Harvey, S. P.; Li, Z.; Christians, J. A.; Zhu, K.; Luther, J. M.; Berry, J. J. Probing Perovskite Inhomogeneity Beyond the Surface: Tof-Sims Analysis of Halide Perovskite Photovoltaic Devices. *ACS Appl. Mater. Interfaces* **2018**, *10* (34), 28541−28552.

(41) Harvey, S. P.; Messinger, J.; Zhu, K.; Luther, J. M.; Berry, J. J. J. A. E. M. Investigating the Effects of Chemical Gradients on Performance and Reliability within Perovskite Solar Cells with Tof-Sims. *Adv. Energy Mater.* **2020**, 1903674.

(42) Lee, J.; Gilmore, I.; Seah, M. Linearity of the Instrumental Intensity Scale in Tof-Sims—a Vamas Interlaboratory Study. *Surf. Interface Anal.* **2012**, *44* (1), 1−14.

(43) Noel, C.; Busby, Y.; Mine, N.; Houssiau, L. Tof-Sims Depth Profiling of Organic Delta Layers with Low-Energy Cesium Ions: Depth Resolution Assessment. *J. Am. Soc. Mass Spectrom.* **2019**, *30* (8), 1537−1544.

(44) Liao, H.-Y.; Tsai, M.-H.; You, Y.-W.; Chang, H.-Y.; Huang, C.-C.; Shyue, J.-J. Dramatically Enhanced Oxygen Uptake and Ionization Yield of Positive Secondary Ions with C60+ Sputtering. *Anal. Chem.* **2012**, *84* (7), 3355−3361.

(45) Brison, J.; Muramoto, S.; Castner, D. G. Tof-Sims Depth Profiling of Organic Films: A Comparison between Single-Beam and Dual-Beam Analysis. *J. Phys. Chem. C* **2010**, *114* (12), 5565−5573.

(46) Moritani, K.; Houzumi, S.; Takeshima, K.; Toyoda, N.; Mochiji, K. Preferential Sputtering of DNA Molecules on a Graphite Surface by Ar Cluster Ion Beam. *J. Phys. Chem. C* **2008**, *112* (30), 11357−11362.

(47) Cumpson, P. J.; Portoles, J. F.; Barlow, A. J.; Sano, N.; Birch, M. Depth Profiling Organic/Inorganic Interfaces by Argon Gas Cluster Ion Beams: Sputter Yield Data for Biomaterials, in-Vitro Diagnostic and Implant Applications. *Surf. Interface Anal.* **2013**, *45* (13), 1859−1868.

(48) Liu, M.; Johnston, M. B.; Snaith, H. J. Efficient Planar Heterojunction Perovskite Solar Cells by Vapour Deposition. *Nature* **2013**, *501* (7467), 395.

(49) Burschka, J.; Pellet, N.; Moon, S.-J.; Humphry-Baker, R.; Gao, P.; Nazeeruddin, M. K.; Grätzel, M. Sequential Deposition as a Route to High-Performance Perovskite-Sensitized Solar Cells. *Nature* **2013**, *499* (7458), 316.

(50) Nie, W.; Tsai, H.; Asadpour, R.; Blancon, J.-C.; Neukirch, A. J.; Gupta, G.; Crochet, J. J.; Chhowalla, M.; Tretiak, S.; Alam, M. A.; et al. High-Efficiency Solution-Processed Perovskite Solar Cells with Millimeter-Scale Grains. *Science* **2015**, *347* (6221), 522−525.

(51) Chen, Q.; Zhou, H.; Song, T.-B.; Luo, S.; Hong, Z.; Duan, H.-S.; Dou, L.; Liu, Y.; Yang, Y. Controllable Self-Induced Passivation of Hybrid Lead Iodide Perovskites toward High Performance Solar Cells. *Nano Lett.* **2014**, *14* (7), 4158−4163.

(52) Brinkmann, K.; Zhao, J.; Pourdavoud, N.; Becker, T.; Hu, T.; Olthof, S.; Meerholz, K.; Hoffmann, L.; Gahlmann, T.; Heiderhoff, R.; et al. Suppressed Decomposition of Organometal Halide Perovskites by Impermeable Electron-Extraction Layers in Inverted Solar Cells. *Nat. Commun.* **2017**, *8*, 13938.

(53) Conings, B.; Drijkoningen, J.; Gauquelin, N.; Babayigit, A.; D'Haen, J.; D'Olieslaeger, L.; Ethirajan, A.; Verbeeck, J.; Manca, J.;

Mosconi, E.; et al. Intrinsic Thermal Instability of Methylammonium Lead Trihalide Perovskite. *Adv. Energy Mater.* **2015**, *5* (15), 1500477.

(54) Busby, Y.; Agresti, A.; Pescetelli, S.; Di Carlo, A.; Noel, C.; Pireaux, J.-J.; Houssiau, L. J. M. t. e. Aging Effects in Interface-Engineered Perovskite Solar Cells with 2d Nanomaterials: A Depth Profile Analysis. *Materials Today Energy* **2018**, *9*, 1−10.

(55) Dong, X.; Fang, X.; Lv, M.; Lin, B.; Zhang, S.; Ding, J.; Yuan, N. Improvement of the Humidity Stability of Organic−Inorganic Perovskite Solar Cells Using Ultrathin Al 2 O 3 Layers Prepared by Atomic Layer Deposition. *J. Mater. Chem. A* **2015**, *3* (10), 5360−5367.

(56) Yoon, S. J.; Draguta, S.; Manser, J. S.; Sharia, O.; Schneider, W. F.; Kuno, M.; Kamat, P. V. Tracking Iodide and Bromide Ion Segregation in Mixed Halide Lead Perovskites During Photo-irradiation. *ACS Energy Lett.* **2016**, *1* (1), 290−296.

(57) Bischak, C. G.; Hetherington, C. L.; Wu, H.; Aloni, S.; Ogletree, D. F.; Limmer, D. T.; Ginsberg, N. S. Origin of Reversible Photoinduced Phase Separation in Hybrid Perovskites. *Nano Lett.* **2017**, *17* (2), 1028−1033.